

A rare case of FR I interaction with a hot X-ray bridge in the A2384 galaxy cluster

V. Parekh^{1,2*}, T. F. Laganá³, K. Thorat^{1,2}, K. van der Heyden⁴, A. Iqbal⁵
and F. Durret⁶

¹*Department of Physics and Electronics, Rhodes University, Grahamstown, Republic of South Africa*

²*South African Radio Astronomy Observatory (SARAO), Cape Town, Republic of South Africa*

³*Núcleo de Astrofísica, Universidade Cruzeiro do Sul/Universidade Cidade de São Paulo,*

R. Galvão Bueno 868, Liberdade, São Paulo, SP, 01506-000, Brazil

⁴*Department of Astronomy, University of Cape Town, Cape Town, Republic of South Africa*

⁵*Raman Research Institute, Sadashiv Nagar, Bangalore, India*

⁶*Sorbonne Université, CNRS, UMR 7095, Institut d'Astrophysique de Paris, 98bis Bd Arago, 75014, Paris, France*

MNRAS accepted.

ABSTRACT

Clusters of varying mass ratios can merge and the process significantly disturbs the cluster environments and alters their global properties. Active radio galaxies are another phenomenon that can also affect cluster environments. Radio jets can interact with the intra-cluster medium (ICM) and locally affect its properties. Abell 2384 (hereafter A2384) is a unique system that has a dense, hot X-ray filament or bridge connecting the two unequal mass clusters A2384(N) and A2384(S). The analysis of its morphology suggests that A2384 is a post-merger system where A2384(S) has already interacted with the A2384(N), and as a result hot gas has been stripped over a ~ 1 Mpc region between the two bodies. We have obtained its 325 MHz GMRT data, and we detected a peculiar FR I type radio galaxy which is a part of the A2384(S). One of its radio lobes interacts with the hot X-ray bridge and pushes the hot gas in the opposite direction. This results in displacement in the bridge close to A2384(S). Based on *Chandra* and *XMM-Newton* X-ray observations, we notice a temperature and entropy enhancement at the radio lobe-X-ray plasma interaction site, which further suggests that the radio lobe is changing thermal plasma properties. We have also studied the radio properties of the FR I radio galaxy, and found that the size and radio luminosity of the interacting north lobe of the FR I galaxy are lower than those of the accompanying south lobe.

Key words: Radio galaxies; clusters of galaxies; intra-cluster medium

1 Introduction

The formation and evolution of galaxy clusters most likely results from complex mergers of multi-component systems. Cluster mergers are highly dynamical processes (Sarazin 2002), and numerous, heterogeneous merger episodes (Ferrari et al. 2006; Poole et al. 2006) are considered to be the most natural physical processes for disturbing both their cool-core and relaxed structure. Even in the present age, clusters are constantly growing by matter accretion at the nodes of large scale filaments of galaxies (Springel et al. 2005; Dolag et al. 2008; Tempel et al. 2014; Bagchi et al. 2017).

Recently, X-ray observations of clusters have shown a

variety of features that are due to either minor or major mergers, such as cold fronts, gas sloshing, substructures, shock edges, etc., (Nurgaliev et al. 2013; Weißmann et al. 2013; Parekh et al. 2015). One of the most evident is a bimodal pair of galaxy clusters, with a hot, dense Mpc scale extended gaseous region between the two clusters taking the form of a filament or bridge (Werner et al. 2008; Akamatsu et al. 2016; Parekh et al. 2017). The imprints of the merger process depend on the masses of the subsystems and on the impact parameter. These bimodal clusters are ideal probes to study the different evolutionary epochs in the formation of clusters, to understand how the merger shocks propagate and dissipate kinetic energy during the cluster merging process, and to explore the intra-cluster medium (ICM) (Ryu et al. 2003; Akahori & Yoshikawa 2010; Planck Collabora-

* E-mail: viralp@ska.ac.za

tion et al. 2013). Murgia et al. (2010) have detected diffuse radio halos among the close pair of each of the clusters A399-A401, which is considered to be a sporadic detection. This radio detection is important to study the origin of diffuse radio halos in connection with the evolutionary stage of the merger. Optical observations also support the scenario of a galaxy filament tracing the hot gaseous bridge between two merging clusters (Mauger et al. 2011).

Joint radio and X-ray analyses show many interesting phenomena taking place in the interaction between radio galaxies and the ICM (Feretti & Venturi 2002; Blanton et al. 2003; Wing & Blanton 2011; Paterno-Mahler et al. 2017). For example, X-ray observations have shown cavities in the ICM of a number of relaxed and cool core clusters. The radio observations of these clusters reveal that these cavities are the result of the interaction of tailed radio galaxies with the X-ray emitting ICM, where the radio bubbles or lobes fill these X-ray cavities (McNamara & Nulsen 2007, 2012, and references therein). The powerful AGN launch radio jets which create cavities and jet outbursts, that are considered to be a feedback mechanism regulating the cooling flow in cool core clusters (Fabian 1994; Peterson & Fabian 2006; Fabian 2012). The two types of plasmas, both thermal and non-thermal, do not mix very well and the jets inflate bubbles in the ICM. Another widely seen example is the ICM exerting pressure on fast moving radio galaxies inside a dense cluster environment. As a result, a wide range of distorted and asymmetric extended morphologies is visible among radio galaxies. In this case, the radio structure in which lobes or plumes are not aligned with the central galaxy can be due to the bending of jets, generally known as bent-tail (BT) radio galaxies (Dehghan et al. 2014). Bent tail source host galaxies are usually non-central to the cluster.

AGN-powered radio galaxies can be classified on a morphological basis into Fanaroff-Riley Class I and II (FR I/FR II henceforth) (Fanaroff & Riley 1974). The classification is defined by the ratio of the distance between the brightest points in the source to the total extent of the source. If this ratio is greater than 0.5 for a given source, the source would be classified as an FR II source; otherwise it would be put in the FR I class. Sources belonging to the FR I class have morphology typified by a comparatively bright core and diffuse, plume-like jets/lobes. FR II sources, on the other hand, show the brightest emission at the ends of their extent (these are called ‘hotspots’). Bent-tail radio sources are predominantly FR I sources that are rapidly moving through the dense ICM and so become distorted.

In this paper, we studied the uncommon phenomenon of the interaction between the radio lobe and the extended thermal X-ray emission in the bimodal A2384 galaxy cluster, where the radio lobe displaces the hot filamentary gas on a large scale. We also studied the thermodynamical properties of the X-ray bridge to understanding the impact of radio emission on the hot thermal gas. Based on the Simbad[†] and NED databases[‡], the redshift of A2384 is $z = 0.0943$ and Maugor et al. (2011) classified it as Abell richness class 1 and BM-type II-III. We selected the A2384 galaxy cluster from Planck Collaboration et al. (2013) and it was

detected in the Planck observation and identified as PLCK-ESZ G033.46-48.43 (Planck Collaboration et al. 2014). This cluster shows a very complex X-ray morphology and a dense ICM between the pair of clusters. The selection of this cluster includes the availability of high-quality *Chandra* and *XMM-Newton* X-ray data and of optical spectroscopic data to identify its member galaxies. A2384 was previously studied in X-rays by Ulmer & Cruddace (1982) with the Einstein satellite, by Henriksen (1996) with ROSAT HRI and by Maugor et al. (2011) with *XMM-Newton*. In all these X-ray observations, the two clusters were found to be separated by a projected ~ 1 Mpc X-ray bridge. Further, Cypriano et al. (2004) and Pranger et al. (2014) performed weak lensing and detailed optical analysis of A2384.

This paper is organised as follows; Section 2 gives a note on the serendipitous discovery of FR I radio galaxy, Section 3 describes the X-ray and radio observations and their data reduction procedures. Section 4 presents our images and results. Section 5 shows the X-ray spectral analysis. Section 6 is the discussion and Section 7 gives the conclusions. We assumed $H_0 = 70 \text{ km s}^{-1} \text{ Mpc}^{-1}$, $\Omega_M = 0.3$ and $\Omega_\Lambda = 0.7$ throughout the paper. At redshift $z = 0.0943$, $1''$ corresponds to 1.75 kpc.

2 Serendipitous discovery of A2384 FR I radio galaxy

Diffuse radio sources in the form of radio halos and relics of the size of ~ 1 Mpc are mostly detected in merging and massive clusters (van Weeren et al. 2019; Feretti et al. 2012). We studied A2384 for two main reasons: (1) to detect diffuse radio emission in the form of a radio halo associated with A2384(N), as it shows disturbed X-ray morphology and (2) to achieve a sensitive low frequency radio observation of the A2384 X-ray bridge region, to detect the magnetic field and relativistic particles in the region between the two merging clusters, as recently detected in the merging clusters A399-A401 with LOFAR data (Govoni et al. 2019). Early radio observations of A2384 were not sensitive enough for our studies. From our newer high quality GMRT data, we discovered a peculiar FR I radio galaxy associated with the A2384 system. In this work, we evaluated the radio properties of a FR I galaxy and its interaction with the ICM of the A2384 bridge.

3 X-ray and Radio observations

3.1 Chandra data analysis

We retrieved *Chandra* archival data (obsid 4202, date of observation 2002-11-18, and total exposure time $\sim 31,445$ sec) to study A2384. We used high-resolution *Chandra* data for both imaging and spectral analysis purposes. For the data reduction, we followed the standard X-ray data analysis procedure. We processed the *Chandra* data with the CIAO (v 4.11 and CALDB 4.8.2) software. In the data reduction steps, we first used the `chandra_repro` task to reprocess ACIS imaging data, followed by removing high background flares (3σ clipping) with the task `lc_sigma_clip`. All filtered event files (exposure time $\sim 31,254$ sec after flare removal) included the 0.3–7 keV broad energy band and $1.968''$ pixel binning. We detected and removed point sources around the cluster and bridge regions using the `wavdetect` and `dmfilth` tasks, respectively. Finally, we divided the count image by the exposure map and generated the flux image

[†] <http://simbad.u-strasbg.fr/simbad/>

[‡] <https://ned.ipac.caltech.edu/>

(photon $\text{cm}^{-2} \text{s}^{-1}$). We also subtracted the background from the flux image using Chandra blank sky files[§].

3.2 XMM-Newton Data Reduction

A2384 was observed on 2004 October 28th for ~ 26 ks for MOS and ~ 19.4 ks for pn (XMM-Newton observation id. 0201902701). Prime full frame mode was used for the three cameras (extended mode for pn) with thin filters. The data reduction was done with SAS version 16.1.0 (July 2017) and calibration files updated to 2019 April. In order to filter background flares, we applied a 2σ -clipping procedure using the light curves in the [10–14] keV energy band. The resulting “cleaned” exposure times are 15.62 ks for MOS cameras and 8.17 ks for pn, respectively. To take into account the background contribution for each detector, we obtained a background spectrum in an outer annulus of the observation in the 10–12 keV energy band. We compared these spectra with the blank sky obtained by Read & Ponman (2003) in the same region and energy band. Then, we rescaled the observation background to the blank sky background to obtain a normalisation parameter that will be used in the spectral fits. Point sources were detected by visual inspection, confirmed in the High Energy Catalogue 2XMMi Source, and excluded from our analysis.

For XMM-Newton imaging purposes, we used the “IMAGES” script[¶] to generate combined MOS1, MOS2 and pn smoothed images. This script works as a pipeline to automatically filter out high background flares, bad pixels and columns, apply exposure corrections and finally combine MOS and pn data for the specified energy bands. We then smoothed these final images.

3.3 Radio data analysis

We observed the A2384 cluster with the upgraded GMRT band 3 (250–500 MHz) in January 2019 for a total duration of ~ 6 hours (P.I. V. Parekh, obsid. 28_087). This u-GMRT observation delivered both the narrow band (325 MHz central frequency with 32 MHz bandwidth) and wideband (400 MHz central frequency with 200 MHz bandwidth) data. The narrow band data were processed with a fully automated pipeline based on the SPAM package (Intema et al. 2009; Intema 2014), which includes direction-dependent calibration, modelling and imaging to suppress mainly ionospheric phase errors. Briefly, the pipeline consists of two parts: (1) a *pre-processing* part that converts the raw data from individual observing sessions into pre-calibrated visibility data sets for all observed pointings, and (2) a *main pipeline* part that converts pre-calibrated visibility data per pointing into Stokes I continuum images. The flux scale is set by calibration on 3C286 using the models from Scaife & Heald (2012). We used different robust weighting and outer tapering values in the IMAGR task to make high and low resolution images. These images are primary beam corrected. More details on the processing pipeline and characteristics of the data products are given in the paper on the first TGSS alternative data release (Intema et al. 2017, ADR1). Our wide band data reduction process is ongoing and we aim to report the corresponding results in our next paper.

4 Images

A2384 is very peculiar cluster system (Maurogordato et al. 2011; Pranger et al. 2014) that displays a dense X-ray filament (~ 700 kpc size) between A2384(N) (North cluster) and A2384(S) (South cluster) (Fig. 1(a)). A2384 is similar to the A3017 (Parekh et al. 2017) and A222-A223 (Werner et al. 2008) cluster systems, which also display X-ray filament between two sub-clusters. The optical data analysis of the galaxy distribution (Maurogordato et al. 2011), at all magnitude limits, also shows a very elongated structure along the north-south axis (Fig. 1(b)). A total of 56 cluster members have been identified, and both the X-ray gas and galaxy distribution approximately define the same bimodal structure. Recently, Pranger et al. (2014) have used 2dF and EFOSC2 spectroscopic data of A2384 and detected another substructure in the east of the central cluster region, which is falling onto the cluster and makes this system even more puzzling. The properties of A2384 are given in Table 1. The X-ray observations show that A2384 is elongated from north to south with a physical size of ~ 1.5 Mpc and an X-ray peak to peak distance of ~ 1.1 Mpc. In the Chandra X-ray map, there is a displacement visible in the X-ray bridge at the distance of ~ 800 kpc from the X-ray peak of A2384(N). At this position, the X-ray gas becomes distorted and bent towards the east. We have marked this by white arrows in Fig. 1(a), and the red line in the same figure shows the projected distance between A2384(N) and A2384(S). The distribution of gas in the bridge is broader ($7'$) up to this displacement and then becomes narrower ($4'$), and connects to A2384(S). Such a displacement is uncommon and is probably noticed here for the first time on such a large scale.

We plotted the 325 MHz GMRT radio contours on the Chandra X-ray image in Fig. 2(a). The FR I radio galaxy located $100''$ north of the BCG (LEDA 67523) of A2384(S) is detected. We classified this galaxy as FR I is based on its morphology. Two lobes extended in the NE-SW direction are associated with the FR I radio galaxy. From the Simbad astronomical database, we found that the counterpart of the FR I radio galaxy is LEDA 851827. The optical position of LEDA 851827 (J2000 RA:21h52m08.1s; Dec:-19d41m27s) matches well its radio counterpart within the $25''$ beam of the 325 MHz GMRT image. The spectroscopic redshift of this galaxy is ~ 0.09447 ; hence, this galaxy is a member of the A2384 cluster. This further supports the observational evidence of the interaction between the NE radio lobe of LEDA 851827 and the X-ray bridge. Maurogordato et al. (2011) also identified this galaxy as a cluster member of A2384 in their optical catalogue. This host radio galaxy also has a counterpart at 1.4 GHz (NVSS 215208-194147) (Condon et al. 1998). However, both radio lobes are absent in the NVSS observation. The physical size of this radio galaxy (from the top to the bottom of the radio lobes) is ~ 830 kpc. The X-ray and radio images show that the NE lobe is displacing the X-ray gas in the east direction and is causing the discontinuity in the X-ray emissivity. We estimated, by visual inspection, that the total gas displacement could be ~ 400 kpc in the east direction from the projected distance between A2384(N) and A2384(S). We also detected a tailed radio galaxy which could be associated with the BCG (LEDA 190740) of A2384(N). Its tail is extending $\sim 1.35'$ (141 kpc) towards the south-east direction.

[§] <http://cxc.harvard.edu/ciao/threads/acisbackground/>
[¶] <https://www.cosmos.esa.int/web/xmm-newton/images>

Table 1. Properties of A2384. For A2384(N) and (S), the positions and redshifts z correspond to the two BCGs. M_{200} taken from Pranger et al. (2014), M_{500} and L_{500} taken from the MCXC catalogue and M_{gas} from this work. M_{SZ} is the Sunyaev–Zel’dovich mass proxy taken from the Planck Collaboration et al. (2014).

Cluster components	RA(J2000) h m s	DEC(J2000) d m s	z	M_{200} $10^{15} M_{\odot}$	M_{500} $10^{14} M_{\odot}$	M_{gas} $10^{13} M_{\odot}$	M_{SZ} $10^{14} M_{\odot}$	L_{500} $10^{44} \text{ erg s}^{-1}$
A2384(N)	21 52 21.9	-19 32 48.6	0.092	1.84	1.30	1.42	-	-
A2384(S)	21 52 09.5	-19 43 23.7	0.096	1.17	0.78	0.86	-	-
A2384(Total)	-	-	0.0943	2.34	2.61	2.84	4.07	1.66

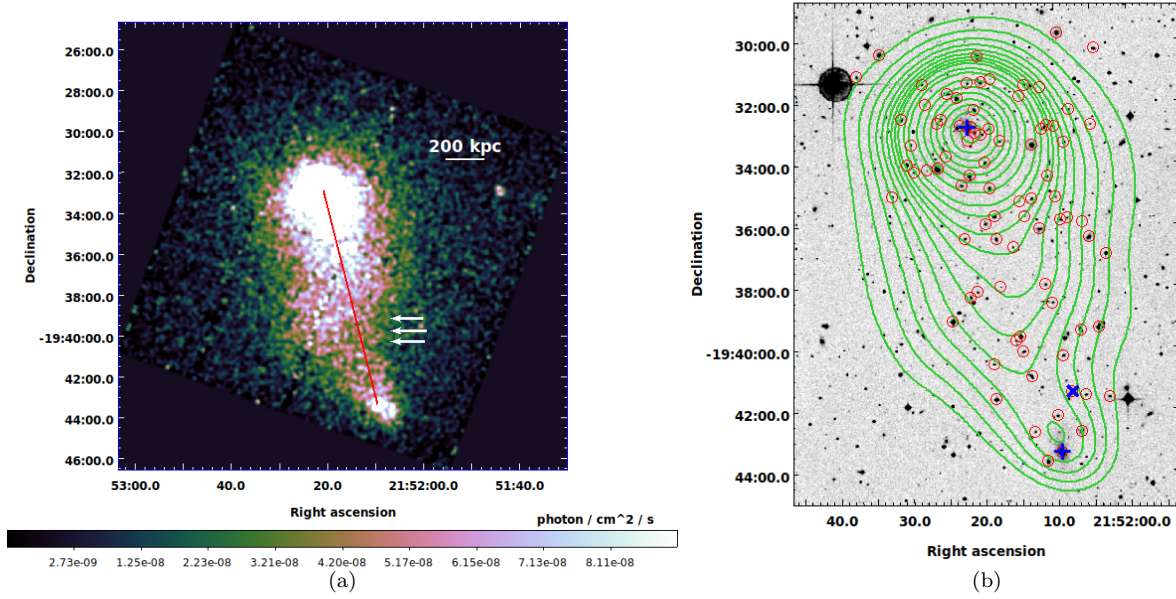


Figure 1: (a) A2384 exposure corrected and background subtracted *Chandra* X-ray image. The white arrows show the notch or displacement location in the X-ray bridge. The red line shows the projected distance between two X-ray peaks. (b) A2384 DSS optical image in grey color. The red circles show the member galaxies from Maurogordato et al. (2011). The green contours show the *Chandra* smoothed ($\sigma = 15''$) X-ray emission. BCGs of A2384(N) and A2384(S) are marked with blue ‘+’ symbols. The LEDA 851827 galaxy is marked with an blue ‘x’.

In the GMRT 325 MHz map, we have an rms of $0.8 \text{ mJy beam}^{-1}$ and a beam size of $25'' \times 25''$. We calculated (1) the north lobe size is $\sim 165'' \times 134''$ and its total integrated flux density $\sim 112 \pm 12 \text{ mJy beam}^{-1}$, (2) the south lobe size is $\sim 240'' \times 220''$ and its total integrated flux density $\sim 173 \pm 18 \text{ mJy beam}^{-1}$, and (3) for the entire FR I radio galaxy, the flux density is $\sim 421 \pm 43 \text{ mJy beam}^{-1}$.

In the ACIS *Chandra* data, there are CCD gaps in the bridge region that could interfere in the analysis. Thus, we also prefer to consider XMM-*Newton* data for A2384, which have different CCD geometries, better sensitivity and larger FOV (field of view) as compared to *Chandra*. We have shown MOS1, MOS2 and pn combined smoothed images in Fig. 2(b) together with radio and DSS optical images. We confirmed that the X-ray properties of the bridge, as mentioned above, in the XMM-*Newton* image are the same as in the *Chandra* observation and there are no observational artefacts which caused the displacement in the X-ray bridge.

4.1 Surface brightness profile

To understand the effect of the radio lobe on the X-ray bridge, we derived the surface brightness (SB) profile along the extended radio lobe direction (NE) (Fig. 3(a)) and the resulting surface brightness profile (Fig. 3(b)). First, we calculated that the total counts within the bridge region are ~ 13744 and the average background counts are ~ 2690 (in the corresponding blank sky image), giving a SNR $_{\parallel}$ of ~ 94 . We used the PROFFIT v1.5 software (Eckert et al. 2011) to derive the profile using an image corrected by the exposure map and point source subtracted (to avoid any contamination). We extracted the photon counts from the green box region, as shown in Fig. 3(a). The total number of counts within the box is ~ 7200 . The selection of the box size and angle were taken from the XMM-*Newton* 2D temperature map (see Section 5.2), where we noticed a high and low temperature distribution across the north lobe. The size of the box ($w \times h$) is $3.8' \times 5'$ and 170° rotation angle with respect to the RA axis. We took bin size is $10''$

$$\parallel \text{ SNR} = \text{Source counts} / \sqrt{\text{Total counts}}$$

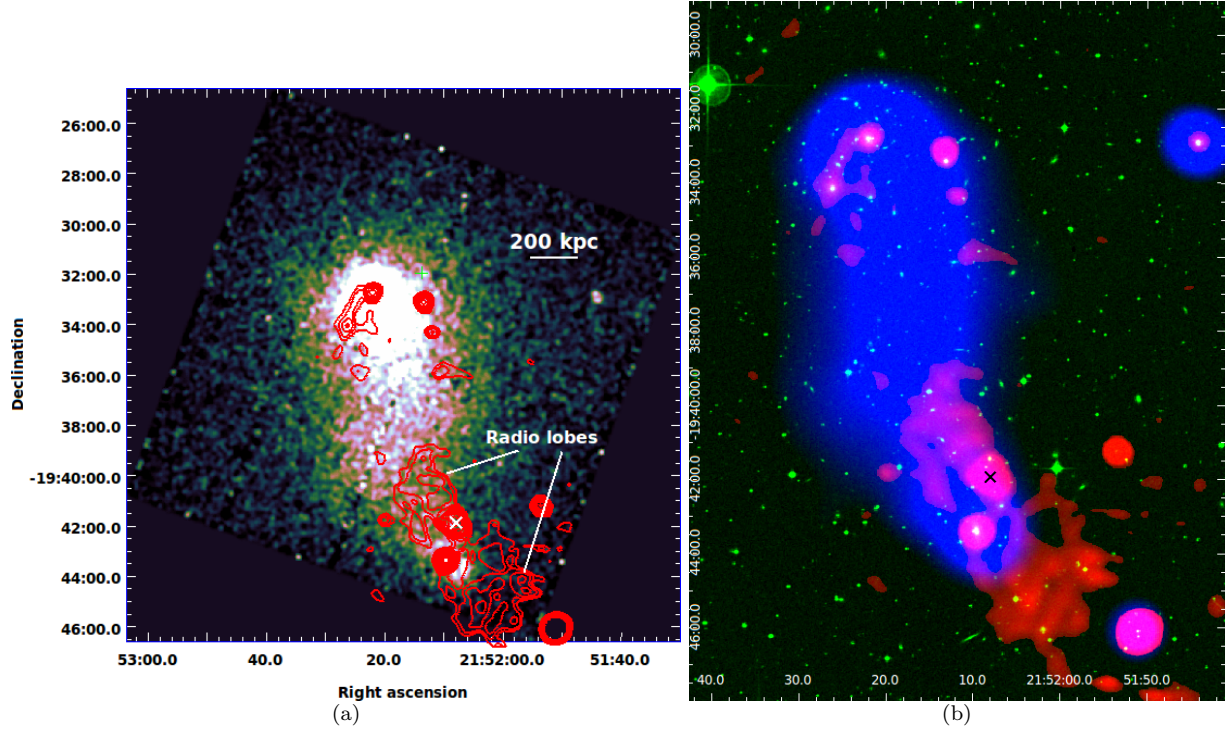


Figure 2: (a) A2384 *Chandra* X-ray color image. The red contours show the GMRT 325 MHz observation. The contours increase in steps of $\sqrt{2}$. The first contour is drawn at 3σ . (b) Red is the radio GMRT 325 MHz (3σ) image, green is the DSS optical image, and blue is the XMM-*Newton* X-ray image of A2384. In both (a) and (b) images the radio galaxy LEDA 851827 is marked with an ‘x’. In the GMRT radio images, the beam size is $25'' \times 25''$ and $1\sigma = 0.8 \text{ mJy beam}^{-1}$.

and then grouped the counts so that each bin has a minimum SNR of 5 and fitted the obtained SB profile with a broken power-law model, as shown in Fig. 3(b). There are five parameters which represent the model: inner slope (Γ_1), outer slope (Γ_2), break radius (\mathcal{R}_{break}), surface brightness or density jump ($n_{e,out}/n_{e,in}$), and normalisation (K). In the fitting process, we kept all parameters free.

$$n_e(R) = \begin{cases} K\eta^{-\Gamma_1}, & \text{if } \eta < \mathcal{R}_{break} \\ K\eta^{-\Gamma_2}, & \text{otherwise} \end{cases} \quad (1)$$

where η is the 3D radius projected on the 2D sky. The best fitting model values are $\Gamma_1 = -0.92 \pm 0.2$, $\Gamma_2 = 0.83 \pm 0.09$, $\mathcal{R}_{break} = 3.2 \pm 0.32$, jump ($n_{e,out}/n_{e,in}$) = 1.09 ± 0.14 and $K = -4.46 \times 10^{-5}$. All these errors are related to fitting procedure errors. The reduced χ^2 is 0.64 for 24 degrees of freedom and probability of 90%. This best-fitted surface brightness model indicates that there is a discontinuity present (\mathcal{R}_{break}), which is coincident with the radio lobe position. This discontinuity is visible $\sim 80\text{--}90''$ (140–160 kpc) away from the outermost contour of the radio lobes. It is located $6'$ and $5.2'$ away from the A2384(N) and A2384(S) X-ray peaks, respectively. We confirmed that the location of \mathcal{R}_{break} or discontinuity and jump fit values are do not vary with the increase the box size in the same direction.

5 Spectral analysis

The spectral analysis was restricted to the energy range [0.7–7.0] keV and all the spectra were grouped to contain a sufficient SNR in each energy bin. In all the fits, the redshift was

fixed at $z = 0.0943$ and the hydrogen column density (N_H) at the Leiden/Argentine/Bonn (LAB) value ($n_H = 3.02 \times 10^{20} \text{ atoms cm}^{-2}$) while the temperature (kT), metallicity (Z), and the spectrum normalisation (K) were free to vary. A single temperature fit was adopted to model the cluster spectrum with an absorbed thermal plasma emission model WABS(APEC). Abundances were measured assuming the ratios from Asplund et al. (2009). For background subtraction, we used blank sky event files after applying the necessary scaling.

If we divide the normalisation by the number of pixels in each bin (K/N_P), we obtain the projected emission measure that is proportional to the square of the electron density n_e^2 , integrated along the line of sight. Thus, with the best-fit temperature and normalisation (K), we estimated the pseudo-entropy (S) and pseudo-pressure (P) in the following ways: $S = kT \times [\frac{K}{N_P}]^{-1/3}$ and $P = kT \times [\frac{K}{N_P}]^{1/2}$.

5.1 Chandra data

For *Chandra* data spectral analysis purposes, we divided the X-ray emission of A2384(N), A2384(S) and bridge into eight regions, as shown in Fig. 4(a) and extracted the spectra from each region. We grouped these spectra such that there is a minimum signal to noise ratio (SNR) of 3 in each bin.

We have plotted kT , S , P , K and abundance (Z) projected radial profiles in Fig. 4(b) and given their best-fit values in Table 3 along with their 68% confidence interval. We also extracted a single spectrum for the X-ray bridge, over a large region, to study its deprojected thermodynamic properties (Fig. 4(a)). We used a box size of ($l \times b$) $290'' \times 430''$ ($508 \times 753 \text{ kpc}^2$) to extract the spectrum.

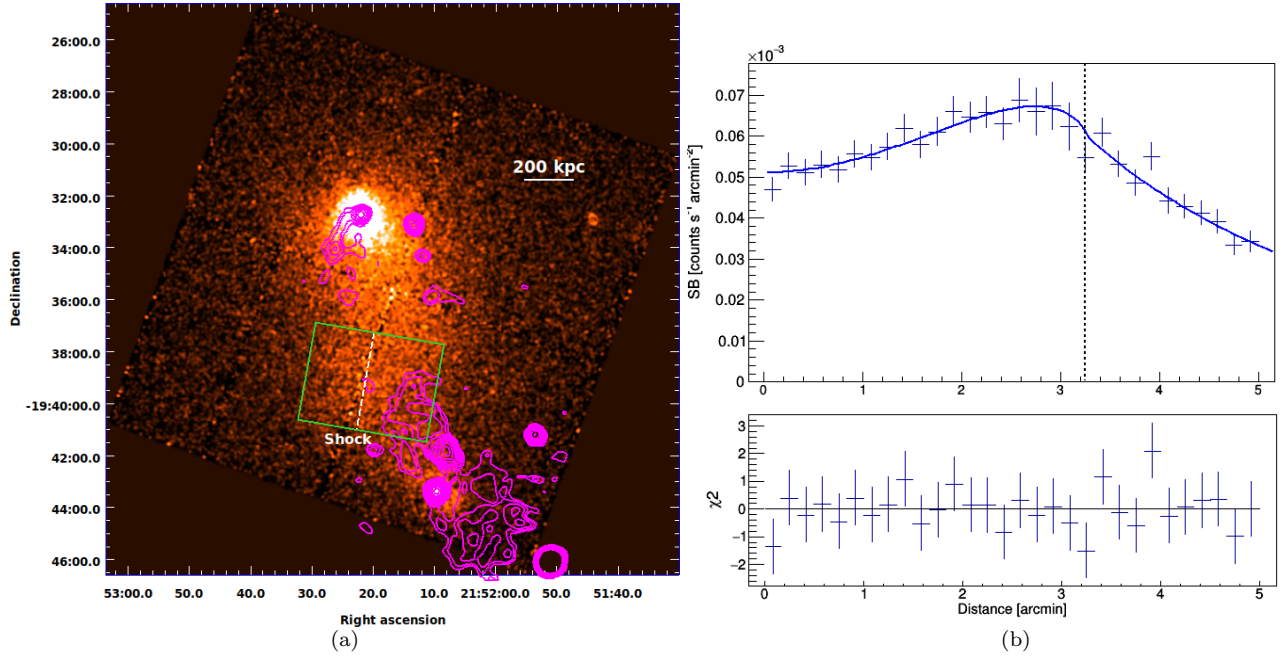


Figure 3: (a) The box region used for extracting surface brightness profile is shown in green, and the white line shows the location of the shock. Magenta contours correspond to the GMRT radio sources, as mentioned in Fig. 2. (b) (Top) resulting X-ray surface brightness profile as a function of distance and (bottom) corresponding χ^2 residuals. The blue line shows the broken power-law best-fit model and the dashed line the location of the shock across the profile.

5.2 XMM-Newton 2D maps

We have derived 2D temperature (kT), pseudo-entropy (S) and pseudo-pressure (P) maps for the A2384 cluster (Fig. 5). We have shown temperature error and reduced χ^2 maps into Appendix Fig. 1. This was achieved by dividing the data into small regions from which spectra were extracted (this procedure was already described in Durret et al. 2010, 2011; Laganá et al. 2008, 2019). For XMM-Newton data, we excluded the energy band from 1.2 to 1.9 keV to avoid any influence from Al and Si instrumental lines. We set a minimum count number of 900 (to assure at least SNR of 30) to each pixel and, if necessary, we increased the region up to a box of 5×5 pixels. Each pixel has a size of 12.8×12.8 arcsec 2 , corresponding to 22.4×22.4 kpc 2 . If we still do not have enough counts after binning, the pixel is ignored and we proceed to the next neighbouring pixel. When we have enough counts, the spectra of MOS1, MOS2 and pn are then simultaneously fitted, and the best kT and Z values are attributed to the central pixel.

6 Discussion

6.1 Dynamical state of A2384

A2384 is a very peculiar, bimodal cluster that is elongated along the north to south direction with a size of ~ 1.5 Mpc. A2384(N) is the most massive cluster of the system. Analysis of the morphology of A2384 can lead to an understanding of its merging stage, evolution and degree of disturbance. To do so, we performed a joint analysis using radio and X-ray data to better understand the radio lobe interaction with the X-ray bridge of A2384. We used three (Gini, M_{20} and Concentration) morphology parameters (Parekh et al. 2015, and references therein) to characterise the dynamical state of A2384(N) and to compare its position with the mor-

phologies of other clusters in the parameter planes. These parameters trace the flux distribution for a given region and their values depend on the degree of disturbance in a given cluster image. We refer the reader to Parekh et al. (2015) for more details about these parameters and their detailed calculation. To calculate these parameters, we considered a 500 kpc region around the centroid of A2384(N). For the purpose of comparing the morphology of A2384 with other clusters, we used data from Parekh et al. (2015) and categorised the dynamical state of each cluster into four stages: strongly relaxed cluster, relaxed cluster, non-relaxed cluster, and strongly non-relaxed cluster, according to the combination of these three parameters. As seen in Fig. 4(c), strongly relaxed clusters are well separated from strongly non-relaxed clusters. A2384(N) falls in the non-relaxed cluster category. The three parameter values (with their uncertainties) are listed in Table 2. Based on the cluster dynamical state separation definitions described in Parekh et al. (2015), the three morphology parameters indicate that A2384(N) is a non-relaxed disturbed cluster. Further, in this analysis, the value of the M_{20} parameter is high as compared with the Gini and Concentration parameters for the same dynamical class of cluster. The Gini and Concentration parameters indicate that A2384 is a non-relaxed cluster (based on its visualisation also it looks like a weak merger), but the higher value of M_{20} suggests that it is strongly non-relaxed. M_{20} is defined as the normalised second-order moment of the brightest 20% of the total cluster flux. In the case of the bimodal cluster A2384, the centroid is located towards the bridge and is $\sim 1.2'$ away from the X-ray peak emission (where 20% of the brightest flux is within only a few pixels). This large distance between the centroid and X-ray peak (due to the bimodal nature of A2384) leads to a higher

Table 2. A2384 morphology parameter values.

Gini	M_{20}	Concentration
0.46 ± 0.0035	-1.34 ± 0.027	1.17 ± 0.009

value of M_{20} . This morphology results could support the scenario that A2384 is a post-merger cluster. The low mass cluster A2384(S) has passed through the more massive cluster A2384(N) and probably stripped it of a large amount of hot gas (and galaxies) along the merger direction.

Further, typically the offset of the BCG from the X-ray peak is consistent with a merging cluster (Mann & Ebeling 2012; Rossetti et al. 2016). The A2384(N) BCG (LEDA 190740) is $10\text{--}15''$ away from the X-ray peak, as also noticed by Maurogordato et al. (2011). We also noticed that the position of A2384(S) BCG (LEDA 67523) is $40''$ far from its X-ray peak. These authors also derived the same conclusion that A2384 is a post-merger cluster seen $\sim 1\text{--}1.5$ Gyr after core collapse. They have also noticed that (1) the velocity dispersion of both subclusters - A2384(N) and (S) - is very high ($\sim 1000 \text{ km s}^{-1}$), and (2) the radial velocity of the BCG of A2384(N) is offset (by $\sim 600 \text{ km s}^{-1}$) from the mean velocity of the member galaxies. These two properties indicate that A2384 is a disturbed system and that the merging has already happened.

6.2 X-ray properties of the bridge

Many clusters show a discontinuity in their X-ray surface brightness profiles, which often indicates the presence of shocks and/or cold fronts (Markevitch & Vikhlinin 2001; Vikhlinin & Markevitch 2002; Markevitch & Vikhlinin 2007). The density jump ($n_{e,\text{out}}/n_{e,\text{in}}$) is considered to be due to the propagation of a shock through the dense gas. We also see a discontinuity in the surface brightness profile across the bridge of A2384, as shown in Fig. 3. This is similar to other merging clusters reported in the literature. In Fig. 3(a), we marked the position of the shock where we observed a discontinuity in the corresponding surface brightness profile (Fig. 3(b)) at a distance of $3.2'$ from the origin of the sector. We derived the Mach number based on the compression factor (or density jump) as:

$$\mathcal{M} = \left(\frac{2C}{\gamma + 1 - (\gamma - 1)C} \right)^{1/2} \quad (2)$$

This gives $\mathcal{M} = 1.06 \pm 0.09$ with the assumption of an adiabatic index for fully ionised plasma of $\gamma = 5/3$ and C is the compression factor. Typically, a powerful merger shock produces a shock wave with \mathcal{M} in the range 2-3 (van Weeren et al. 2019). However, in the case of the A2384 X-ray bridge, we found a low Mach number. This could be due to a weak shock propagated by the radio lobe of the FR I galaxy. Blanton (2004) has reported a weak shock with \mathcal{M} of ~ 1.27 in the cool core Hydra A cluster. Recently Cuciti et al. (2018); Wilber et al. (2019) also reported weak shock propagation in several clusters.

To study the thermodynamic properties of the bridge, we considered a total of 8 regions along the A2384 north to south extended area (Fig. 4(a)) and examined the spectral

properties within each of the zones using *Chandra* data. The temperature varies between ~ 3 and 4 keV from regions 1 to 6. Regions 1 and 2 correspond to the A2384(N). Region 3 is the overlap between the A2384(N) and bridge. The average temperature of A2384(N) is $\sim 3.8 \text{ keV}$. The temperature is higher in region 4, which is a part of the bridge. Regions 5 and 6 correspond to the radio-lobe/ICM interaction site where the temperature is $\sim 4.47 \text{ keV}$ in region 6 and drops in region 5 ($\sim 3.3 \text{ keV}$). Region 6, which has the highest temperature, is the narrowest region of the bridge. Regions 7 and 8 correspond to A2384(S) and have an average temperature of $\sim 2.1 \text{ keV}$. Maurogordato et al. (2011) estimated the temperatures (based on XMM-Newton data) of A2384(N) and (S) to be $\sim 3\text{--}4 \text{ keV}$, the surrounding gas residing in the bridge being hotter, with a temperature up to $4\text{--}5 \text{ keV}$. This previous finding is similar to our temperature estimation.

The normalisation parameter and pressure both decrease in the bridge regions. However, there is an indication that the entropy increases in the bridge regions and maximum at region 6. This indicates that the FR I radio lobe has supplied energy to the hot X-ray plasma. This adiabatic non-thermal heating could deposit energy into the hot gas, causing the entropy to increase in the interaction region. We also plotted the metallicity distribution in A2384, and found a solar abundance of $\sim 0.1\text{--}0.2 Z_{\odot}$ in the bridge region. However, due to poor counts, there is a large uncertainties with metallicity estimations.

Apart from the projected radial profile, we also derived the de-projected thermodynamic properties of the bridge region: the temperature $\sim 4.11^{+0.17}_{-0.17} \text{ keV}$, abundance $\sim 0.22^{+0.09}_{-0.08} Z_{\odot}$, entropy $S \sim 353^{+11}_{-11} \text{ keV cm}^2$, pressure $P \sim 4.82^{+0.272}_{-0.266} \times 10^{-3} \text{ keV cm}^{-3}$, electron density $n_e \sim 1.17^{+0.016}_{-0.016} \times 10^{-3} \text{ cm}^{-3}$ and integrated mass $\sim 0.56^{+0.008}_{-0.008} \times 10^{13} M_{\odot}$. We also estimated the luminosity of the bridge to be $\sim 9.22 \times 10^{43} \text{ erg s}^{-1}$. To calculate these values, we assumed the volume of the filament to be a cylinder ($\pi r^2 h$) of size $145''(\text{r}) \times 430''(\text{h})$ ($254 \times 753 \text{ kpc}^3$). Then we calculated the electron density as:

$$n_e = \sqrt{\frac{\text{Norm} \times 4\pi \times D_A^2 \times (1+z)^2 \times 10^{14}}{\text{Volume} \times 1.18}} \quad (3)$$

where D_A is the angular diameter distance to the source (cm), Norm is the normalisation factor and 1.18 is the electron to proton ratio (n_e/n_p). The integrated total mass within the bridge is calculated as $m_N n_e V$ where m_N is the average nucleon mass per hydrogen atom ($2.12 \times 10^{-24} \text{ g/atom}$), n_e the electron density (cm^{-3}) and V the volume of the cylinder (cm^3).

We generated 2D thermodynamic maps of A2384 based on XMM-Newton data as shown in Fig. 5. There is a arc of the size $\sim 3.8'$ visible in the temperature and entropy maps where temperature and entropy are high. This arc well overlaps with the north radio lobe of FR I galaxy. There is currently no evidence that the FR I radio source is strongly shocking the ICM, but the possibility of weaker shocks cannot be ruled out. If we assume a weak shock is propagating in the direction of the radio lobe extension (north-east), then we can estimate the mean temperature within the lobe region, $T_{\text{post}} \sim 4.4 \pm 0.5 \text{ keV}$ and outside of the lobe region, $T_{\text{pre}} \sim 3.5 \pm 0.3 \text{ keV}$. These values are similar to the temperature values derived from the *Chandra* data (Regions 5 and 6 in Fig. 4(a)). The standard Rankine-Hugoniot model

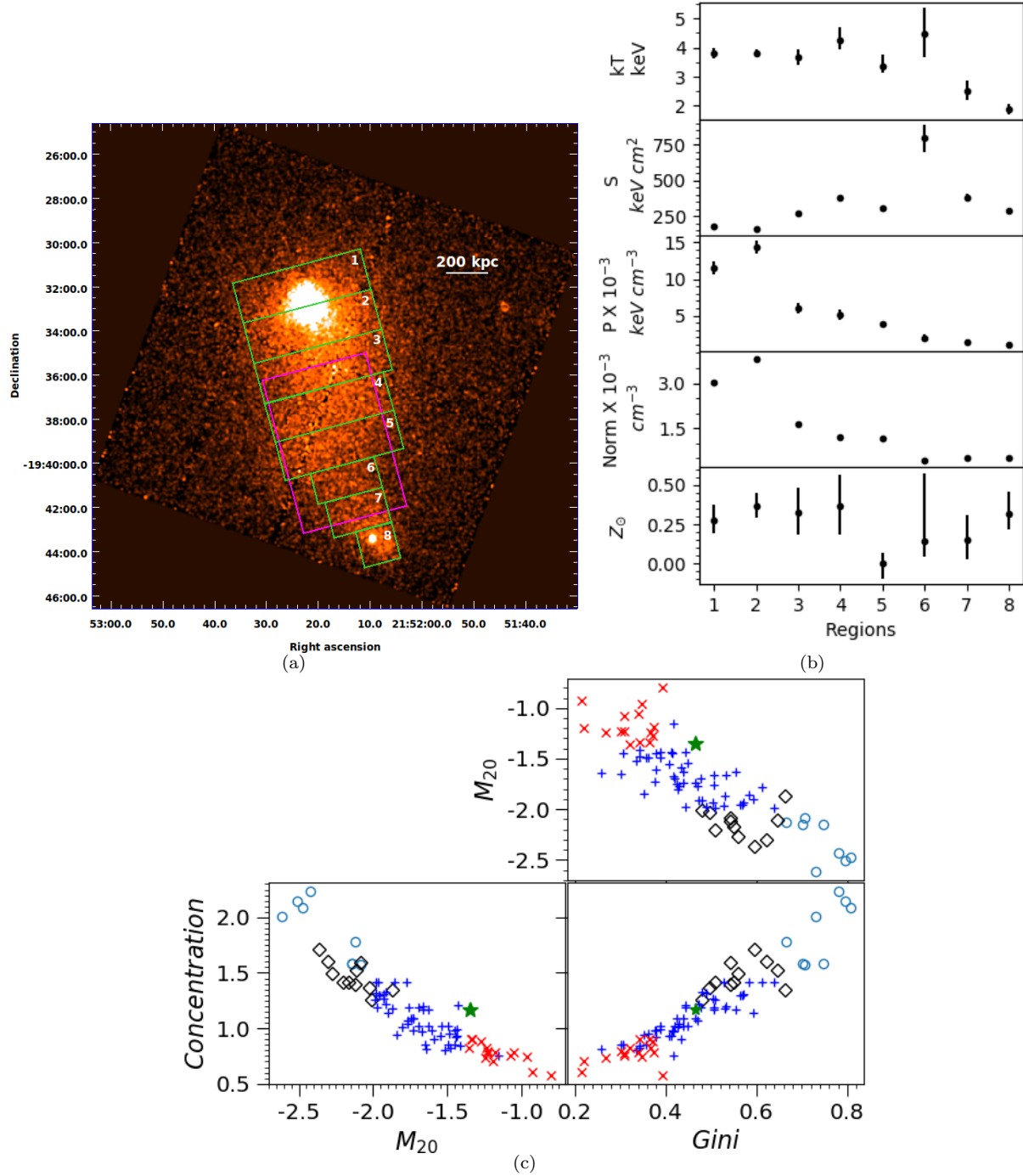


Figure 4: (a) Regions used to extract the spectra from *Chandra* data. The green boxes (marked 1 to 8) and the magenta box were considered to obtain projected and de-projected spectral values. (b) Projected spectral profiles for regions 1 to 8. (c) Three morphology parameters plotted in the parameter-parameter planes. \circ = strongly relaxed (strong cool core) clusters; \diamond = relaxed (cool core) clusters; $+$ = non-relaxed (weak cool core) clusters; and \times = strongly non-relaxed (non-cool core) clusters. A2384(N) is marked with \star . See text for details.

predicts the temperature jump condition:

$$\frac{T_{post}}{T_{pre}} = \frac{[2\gamma\mathcal{M}^2 - (\gamma - 1)][(\gamma - 1)\mathcal{M}^2 + 2]}{(\gamma + 1)\mathcal{M}^2} \quad (4)$$

This leads to a threshold on the Mach number $\mathcal{M} \sim 1.25 \pm 0.035$ with the assumption of an adiabatic index of $\gamma = 5/3$. This Mach number value is close to that derived from

the surface brightness profile of the *Chandra* image (within the error bar). There is also good agreement between the position of the shock in the *Chandra* emissivity map and the *XMM-Newton* temperature map. The pressure map also shows high values around the radio lobe (towards the north direction), which could be due to the impelling of the ICM

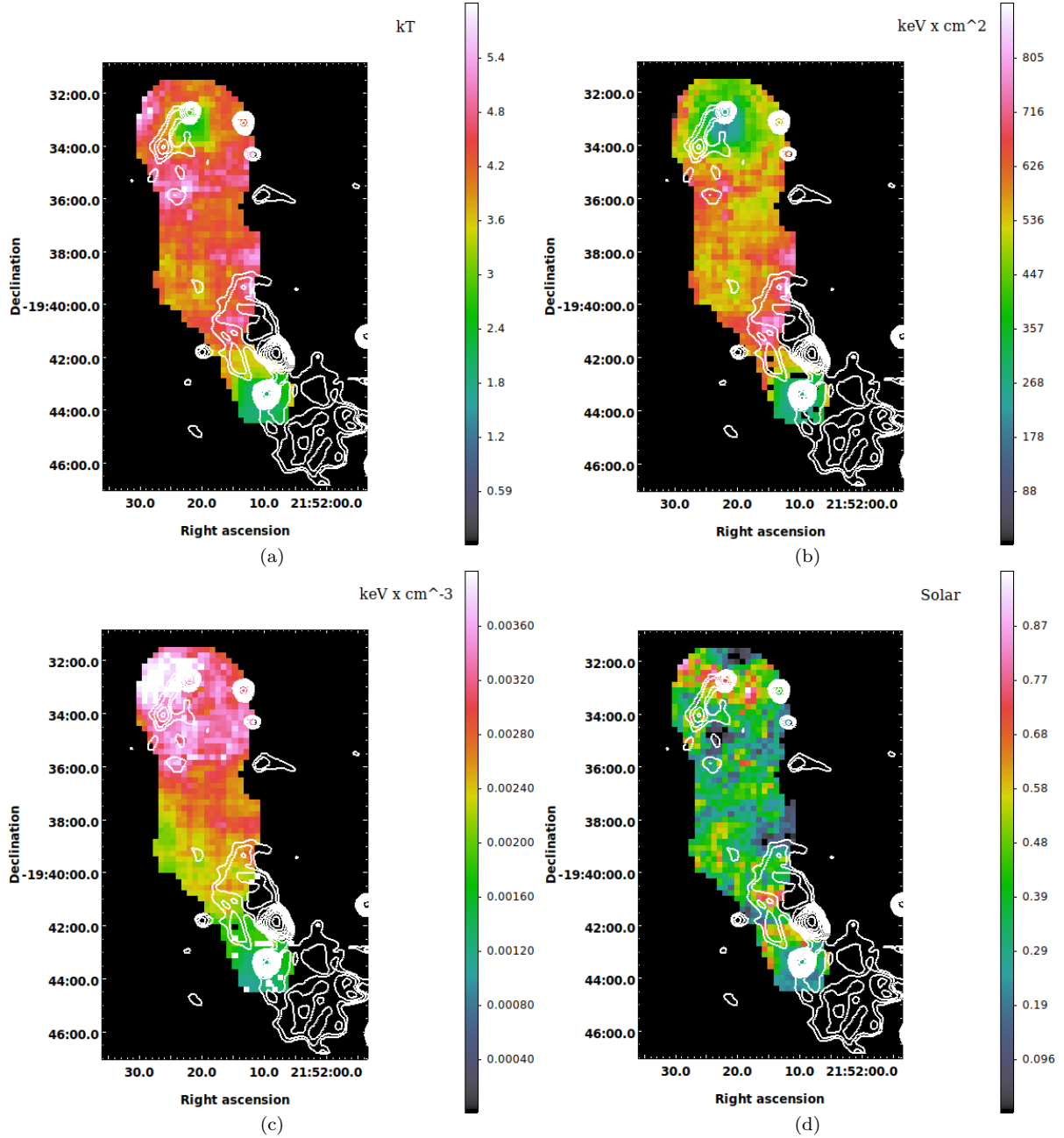


Figure 5: Thermodynamic maps derived from XMM-Newton data. (a) Temperature map, (b) entropy (S) map, (c) pressure (P) map and (d) metallicity (Z) map. The white contours are those of the 325 MHz radio image as in Fig. 2.

by the radio lobe. In the XMM-Newton metallicity map, the solar abundance values in the bridge region are higher than those derived from Chandra data.

Accretion shocks heat the cluster outskirts ($> R_{200}$) (Molnar et al. 2009) raising entropies above 1000 keV cm^2 . This entropy is expected to increase further out to the virial radius. In the A2384 case, the overall low entropy of the bridge suggests that the radiating hot gas in the A2384 bridge has not yet been reached by the shock-heating operating on the ICM in the cluster outskirts, but there could be a localised entropy enhancement due to the radio lobe interaction.

6.3 Masses of the A2384 substructures

Pranger et al. (2014) and Maurogordato et al. (2011) tried to estimate the masses of A2384 (total) and its subclusters. These mass calculations are based on velocity dispersions. A2384 is a disturbed system, so the velocity distribution of this system is largely affected by the cluster merging effect. Observations and simulations both have shown that during the cluster merging process the kinematics of galaxies of an entire cluster system can be strongly boosted (by a factor of ~ 2) and large scale gas motion energy (of colliding clusters) is converted into random motion of the galaxies (Pratt et al. 2019, and reference therein). This results in a significant mass overestimation for a merging system. Pranger et al.

(2014) and Maurogordato et al. (2011) have also noted this problem in their mass calculations, due to the overestimation of the velocity dispersion in A2384. Hence, the mass of A2384 is overestimated and the mass ratio of the A2384(N) and A2384(S) subclusters is an upper limit.

The mass of A2384, as reported in the MCXC catalogue (Piffaretti et al. 2011), is $M_{500} \sim 2.61 \times 10^{14} M_{\odot}$. This is the total mass (within r_{500}^{**}) of the cluster (derived from the Mass-Luminosity scaling relation) which includes dark matter, X-ray gas and stellar mass. To calculate the gas mass, we used the Vikhlinin et al. (2009) sample and the M_{500} - M_{gas} scaling relation given in Table 3 of that paper††. From this, we estimated that the gas mass of the entire A2384 system is $M_{gas, total} \sim 2.84 \pm 0.09 \times 10^{13} M_{\odot}$. After subtracting the gas mass of the bridge computed in the previous section, $M_{gas, bridge}$, from the total gas mass of A2384, we find $M_{gas, N+S} \sim 2.28 \pm 0.08 \times 10^{13} M_{\odot}$, which includes only the gas masses of A2384(N) and (S). This implies that the gas mass of the X-ray bridge is ~ 4 times lower than that of A2384 (N+S).

Pranger et al. (2014) reported that the total masses of A2384(N) and A2384(S) are $M_{200} \sim 1.84 \times 10^{15} M_{\odot}$ and $\sim 1.17 \times 10^{15} M_{\odot}$, respectively. Hence, their mass ratio is 1.6:1. If we assume the same mass ratio for the X-ray gas, then M_{gas} of A2384(N) is $\sim 1.42 \pm 0.05 \times 10^{13} M_{\odot}$, that is ~ 2.5 times higher than the mass of the X-ray bridge. The gas mass of A2384(S) is $\sim 0.86_{-0.03}^{+0.02} \times 10^{13} M_{\odot}$, that is ~ 1.5 times higher than the mass of the X-ray bridge. From the MCXC catalogue, the total luminosity (L_{500}) of the A2384 system is $1.66 \times 10^{44} \text{ erg s}^{-1}$. Hence, the luminosity of the bridge is roughly 1.8 times lower than that of the entire A2384 system.

6.4 Impact of the radio lobe on the X-ray bridge

Combined radio, X-ray and optical observations often show that the fast motion of the (active) radio galaxies and the interaction of the radio jet outflows with the ICM result in an asymmetry in the alignment of the radio lobes. The dense ICM can change the morphology and physical nature of the radio lobes via exerting ram pressure. In the case of A2384 the FR I radio galaxy LEDA 851827 pushes the ICM in the east direction through one of its lobes, as opposed to the jet bending scenario where the ICM distorts the radio jets. Here the radio lobe exerts a mechanical work on the X-ray bridge and displaces the hot and dense gas, and finally, it could be mixed with the surrounding medium and deposit cosmic rays and magnetic energy in the ICM (McNamara & Nulsen 2012).

The radial velocity of LEDA 851827 is $28,321 \pm 18 \text{ km s}^{-1}$ (Pranger et al. 2014), which is close to the radial velocity ($28,696 \pm 53 \text{ km s}^{-1}$) of the BCG of A2384(S), and seems to be associated with the A2384(S) cluster. From NVSS (1400 MHz), we estimate the flux density of the radio galaxy core to be $30 \pm 0.34 \text{ mJy}$. In the 325 MHz GMRT observation, the flux density is $116 \pm 7.3 \text{ mJy}$. This gives a spectral index α ($S_{\nu} \propto \nu^{\alpha}$) $\alpha_{325 \text{ MHz}}^{1400 \text{ MHz}} \sim -0.92$ for the host radio galaxy. We used CASA's IMFIT task to estimate the integrated flux

density of the radio galaxy core. Its position is slightly away from the X-ray emission ($100''$), and north of the BCG of A2384(S). We estimated the radio luminosity as $P = 4\pi D_L^2 S_{\nu}$ where D_L is the luminosity distance at the cluster redshift and S_{ν} the total integrated flux density of the source at the given frequency ν . We measured the total radio luminosity of the north lobe (which interacts with the ICM) to be $P_{325 \text{ MHz}} \sim 2.5 \times 10^{28} \text{ erg s}^{-1} \text{ Hz}^{-1}$. We extrapolated this to 1400 MHz with a spectral index of -0.92 , assuming the same spectral index as the radio galaxy core, and obtained $P_{1400 \text{ MHz}} \sim 6.5 \times 10^{27} \text{ erg sec}^{-1} \text{ Hz}^{-1}$. We estimated the radio luminosity of the south lobe to be $P_{325 \text{ MHz}} \sim 3.8 \times 10^{28} \text{ erg sec}^{-1} \text{ Hz}^{-1}$ and $P_{1400 \text{ MHz}} \sim 1.0 \times 10^{28} \text{ erg sec}^{-1} \text{ Hz}^{-1}$. The south lobe is ~ 1.5 times more luminous than and roughly twice as large as the north lobe. This could suggest that the size of the north lobe is smaller because of its interaction with the ICM and the lobe cannot expand due to the opposite pressure exerted on it by the surrounding dense ICM.

More radio observations of cluster filaments are needed to understand how the shocks (internal and external) govern the large scale structure formation process (Miniati et al. 2000; Ryu et al. 2003; Pfrommer et al. 2006). It is essential to investigate the presence of non-thermal structures beyond the Mpc scale of clusters and to link them with lower density regions. Edwards et al. (2010) reported the first discovery of a bent double lobe radio source (DLRS) between A1763 and A1770 clusters' filament. They used properties of the radio source to constrain the density of the surrounding interfilament medium. The extended radio lobe which interacts with the X-ray bridge or filament between A2384(N) and A2384(S) is a unique detection, and it can be used to set the limits on the pressure of the hot gas, shock structures and large scale magnetic fields.

6.5 Future radio observations

It is important to derive the dynamical age of the interacting radio galaxy of A2384 to understand its evolution with respect to the ICM, the active cycles of the galactic nuclei, and the physical state of the surrounding galactic and intergalactic medium, which allows the launch and propagation of jets. In a follow-up analysis of the low frequency wideband uGMRT data, we plan to model the radio lobes. We also need high-frequency wideband radio data to study the shape of the spectrum along the radio lobes and to conduct the classical spectral-ageing analysis (Harwood et al. 2016, 2017).

7 Conclusions

In this paper, we studied the X-ray properties of the A2384 bridge - a high density region extended between the clusters A2384(N) and A2384(S). We have also shown GMRT radio observations of this system and found radio-X-ray interaction at the cluster outskirts. The north lobe of the FR I radio galaxy displaces the hot gas on a large scale in the bridge region. X-ray cavities are the classic example of radio-X-ray interaction, but in this rare case, this interaction happens in the cluster outskirts region. Further, unlike bent-tail radio galaxies, the FR I radio galaxy causes a displacement in the X-ray gas bridge region. Based on thermodynamic 1D profiles (*Chandra*) and 2D maps (*XMM-Newton*), the entropy increases at the the radio-lobe/ICM interaction site, which

** the characteristic radius within which the mean over-density of the cluster is 500 times the critical density at the cluster redshift
 †† $f_g = M_{gas}/M_{500} = [(0.0764 \pm 0.004)h^{-1.5} + (0.037 \pm 0.006) \times \log(M_{500}/10^{15})]$

Table 3. Spectral properties of the A2384.

Region	T keV	Normalisation $\times 10^{-3} \text{ cm}^{-3}$	Z_{\odot}	S keV cm^2	P keV cm^{-3}	χ^2/dof $\times 10^{-3}$
1	$3.81^{+0.18}_{-0.18}$	$3.030^{+0.092}_{-0.091}$	$0.28^{+0.09}_{-0.09}$	$182^{+4.83}_{-5.05}$	$11.556^{+0.915}_{-0.877}$	119/190
2	$3.80^{+0.14}_{-0.14}$	$3.783^{+0.094}_{-0.094}$	$0.37^{+0.08}_{-0.08}$	$156^{+3.28}_{-3.37}$	$14.372^{+0.914}_{-0.887}$	131/212
3	$3.67^{+0.28}_{-0.26}$	$1.629^{+0.082}_{-0.082}$	$0.32^{+0.16}_{-0.14}$	$265^{+10.64}_{-10.47}$	$5.983^{+0.774}_{-0.709}$	98/147
4	$4.26^{+0.41}_{-0.32}$	$1.205^{+0.064}_{-0.063}$	$0.36^{+0.20}_{-0.18}$	$376^{+22.46}_{-15.42}$	$5.138^{+0.799}_{-0.630}$	91/128
5	$3.36^{+0.37}_{-0.23}$	$1.145^{+0.042}_{-0.040}$	$0.00^{+0.06}_{-0.10}$	$307^{+25.98}_{-14.24}$	$3.853^{+0.582}_{-0.388}$	65/109
6	$4.47^{+0.88}_{-0.79}$	$0.417^{+0.040}_{-0.044}$	$0.14^{+0.44}_{-0.10}$	$800^{+101.33}_{-90.09}$	$1.865^{+0.578}_{-0.489}$	33/50
7	$2.50^{+0.35}_{-0.29}$	$0.530^{+0.051}_{-0.049}$	$0.15^{+0.16}_{-0.12}$	$381^{+27.56}_{-21.82}$	$1.323^{+0.329}_{-0.262}$	29/51
8	$1.88^{+0.15}_{-0.16}$	$0.539^{+0.053}_{-0.051}$	$0.32^{+0.14}_{-0.10}$	$284^{+4.63}_{-6.98}$	$1.014^{+0.191}_{-0.176}$	32/45

indicates the transportation of non-thermal energy to the thermal plasma. Furthermore, the high surrounding pressure suggests a displacement of hot gas. We also derived Mach numbers based on the surface brightness profile and temperature maps, which suggest the presence of a weak shock due to the radio lobe interaction. To better understand this system, we need more radio data at multiple frequencies.

Acknowledgments

VP and KT acknowledge the SKA SA Fellowship. TFL acknowledges financial support from the Brazilian agencies FAPESP and CNPq through grants 2018/02626-8 and 303278/2015-3, respectively. FD is grateful to CNES for long-term support. We would like to thank the anonymous referee for his/her carefully reading our manuscript and for giving such constructive comments which substantially helped improving the quality of the paper. This research has made use of the data from *Chandra* Archive and of software provided by the *Chandra* X-ray Centre (CXC) in the application packages CIAO, ChIPS, and Sherpa. Based on observations obtained with XMM-Newton, an ESA science mission with instruments and contributions directly funded by ESA Member States and NASA. We thank the staff of the GMRT who have made these observations possible. GMRT is run by the National Centre for Radio Astrophysics of the Tata Institute of Fundamental Research.

REFERENCES

Akatori T., Yoshikawa K., 2010, *PASJ*, **62**, 335
Akamatsu H., et al., 2016, *A&A*, **593**, L7
Asplund M., Grevesse N., Sauval A. J., Scott P., 2009, *ARA&A*, **47**, 481
Bagchi J., Sankhyayan S., Sarkar P., Raychaudhury S., Jacob J., Dabhade P., 2017, *ApJ*, **844**, 25
Blanton E. L., 2004, in Reiprich T., Kempner J., Soker N., eds, *The Riddle of Cooling Flows in Galaxies and Clusters of galaxies*. (arXiv:astro-ph/0402342)
Blanton E. L., Gregg M. D., Helfand D. J., Becker R. H., White R. L., 2003, *AJ*, **125**, 1635
Condon J. J., Cotton W. D., Greisen E. W., Yin Q. F., Perley R. A., Taylor G. B., Broderick J. J., 1998, *AJ*, **115**, 1693
Cuciti V., Brunetti G., van Weeren R., Bonafede A., Dallacasa D., Cassano R., Venturi T., Kale R., 2018, *A&A*, **609**, A61
Cypriano E. S., Sodré Jr. L., Kneib J.-P., Campusano L. E., 2004, *ApJ*, **613**, 95
Dehghan S., Johnston-Hollitt M., Franzen T. M. O., Norris R. P., Miller N. A., 2014, *AJ*, **148**, 75
Dolag K., Bykov A. M., Diaferio A., 2008, *Space Sci. Rev.*, **134**, 311
Durret F., Laganá T. F., Adami C., Bertin E., 2010, *A&A*, **517**, A94
Durret F., Laganá T. F., Haider M., 2011, *A&A*, **529**, A38

Eckert D., Molendi S., Paltani S., 2011, *A&A*, **526**, A79
Edwards L. O. V., Fadda D., Frayer D. T., 2010, *ApJ*, **724**, L143
Fabian A. C., 1994, *ARA&A*, **32**, 277
Fabian A. C., 2012, *ARA&A*, **50**, 455
Fanaroff B. L., Riley J. M., 1974, *MNRAS*, **167**, 31P
Feretti L., Venturi T., 2002, in Feretti L., Gioia I. M., Giovannini G., eds, *Astrophysics and Space Science Library* Vol. 272, *Merging Processes in Galaxy Clusters*. pp 163–195, doi:10.1007/0-306-48096-4_6
Feretti L., Giovannini G., Govoni F., Murgia M., 2012, *A&ARv*, **20**, 54
Ferrari C., Arnaud M., Ettori S., Maurogordato S., Rho J., 2006, *A&A*, **446**, 417
Govoni F., et al., 2019, *Science*, **364**, 981
Harwood J. J., et al., 2016, *MNRAS*, **458**, 4443
Harwood J. J., et al., 2017, *MNRAS*, **469**, 639
Henriksen M. J., 1996, in Zimmermann H. U., Trümper J., Yorke H., eds, *Röntgenstrahlung from the Universe*. pp 587–588
Intema H. T., 2014, ArXiv e-prints:1402.4889,
Intema H. T., van der Tol S., Cotton W. D., Cohen A. S., van Bemmelen I. M., Röttgering H. J. A., 2009, *A&A*, **501**, 1185
Intema H. T., Jagannathan P., Mooley K. P., Frail D. A., 2017, *A&A*, **598**, A78
Laganá T. F., Lima Neto G. B., Andrade-Santos F., Cypriano E. S., 2008, *A&A*, **485**, 633
Laganá T. F., Durret F., Lopes P. A. A., 2019, *MNRAS*, **484**, 2807
Mann A. W., Ebeling H., 2012, *MNRAS*, **420**, 2120
Markevitch M., Vikhlinin A., 2001, *ApJ*, **563**, 95
Markevitch M., Vikhlinin A., 2007, *Phys. Rep.*, **443**, 1
Maurogordato S., Sauvageot J. L., Bourdin H., Cappi A., Benoist C., Ferrari C., Mars G., Houairi K., 2011, *A&A*, **525**, A79
McNamara B. R., Nulsen P. E. J., 2007, *ARA&A*, **45**, 117
McNamara B. R., Nulsen P. E. J., 2012, *New Journal of Physics*, **14**, 055023
Miniati F., Ryu D., Kang H., Jones T. W., Cen R., Ostriker J. P., 2000, *ApJ*, **542**, 608
Molnar S. M., Hearn N., Haiman Z., Bryan G., Evrard A. E., Lake G., 2009, *ApJ*, **696**, 1640
Murgia M., Govoni F., Feretti L., Giovannini G., 2010, *A&A*, **509**, A86
Nurgaliev D., McDonald M., Benson B. A., Miller E. D., Stubbs C. W., Vikhlinin A., 2013, *ApJ*, **779**, 112
Parekh V., van der Heyden K., Ferrari C., Angus G., Holwerda B., 2015, *A&A*, **575**, A127
Parekh V., Durret F., Padmanabh P., Pandge M. B., 2017, *MNRAS*, **470**, 3742
Paterno-Mahler R., Blanton E. L., Brodwin M., Ashby M. L. N., Golden-Marx E., Decker B., Wing J. D., Anand G., 2017, *ApJ*, **844**, 78
Peterson J. R., Fabian A. C., 2006, *Phys. Rep.*, **427**, 1
Pfrommer C., Springel V., Enßlin T. A., Jubelgas M., 2006, *MNRAS*, **367**, 113

- Piffaretti R., Arnaud M., Pratt G. W., Pointecouteau E., Melin J.-B., 2011, *A&A*, **534**, A109
- Planck Collaboration et al., 2013, *A&A*, **550**, A134
- Planck Collaboration et al., 2014, *A&A*, **571**, A29
- Poole G. B., Fardal M. A., Babul A., McCarthy I. G., Quinn T., Wadsley J., 2006, *MNRAS*, **373**, 881
- Pranger F., Böhm A., Ferrari C., Maurogordato S., Benoist C., Höller H., Schindler S., 2014, *A&A*, **570**, A40
- Pratt G. W., Arnaud M., Biviano A., Eckert D., Ettori S., Nagai D., Okabe N., Reiprich T. H., 2019, *Space Science Reviews*, **215**, 25
- Read A. M., Ponman T. J., 2003, *A&A*, **409**, 395
- Rossetti M., et al., 2016, *MNRAS*, **457**, 4515
- Ryu D., Kang H., Hallman E., Jones T. W., 2003, *ApJ*, **593**, 599
- Sarazin C. L., 2002, in Feretti L., Gioia I. M., Giovannini G., eds, *Astrophysics and Space Science Library* Vol. 272, *Merging Processes in Galaxy Clusters*. pp 1–38, doi:10.1007/0-306-48096-4_1
- Scaife A. M. M., Heald G. H., 2012, *MNRAS*, **423**, L30
- Springel V., et al., 2005, *Nature*, **435**, 629
- Tempel E., Stoica R. S., Martínez V. J., Liivamägi L. J., Castellan G., Saar E., 2014, *MNRAS*, **438**, 3465
- Ulmer M. P., Cruddace R. G., 1982, *ApJ*, **258**, 434
- Vikhlinin A. A., Markevitch M. L., 2002, *Astronomy Letters*, **28**, 495
- Vikhlinin A., et al., 2009, *ApJ*, **692**, 1033 (V09)
- Weißmann A., Böhringer H., Šuhada R., Ameglio S., 2013, *A&A*, **549**, A19
- Werner N., Finoguenov A., Kaastra J. S., Simionescu A., Dietrich J. P., Vink J., Böhringer H., 2008, *A&A*, **482**, L29
- Wilber A., et al., 2019, *A&A*, **622**, A25
- Wing J. D., Blanton E. L., 2011, *AJ*, **141**, 88
- van Weeren R. J., de Gasperin F., Akamatsu H., Brügggen M., Feretti L., Kang H., Stroe A., Zandanel F., 2019, *Space Sci. Rev.*, **215**, 16

Appendix

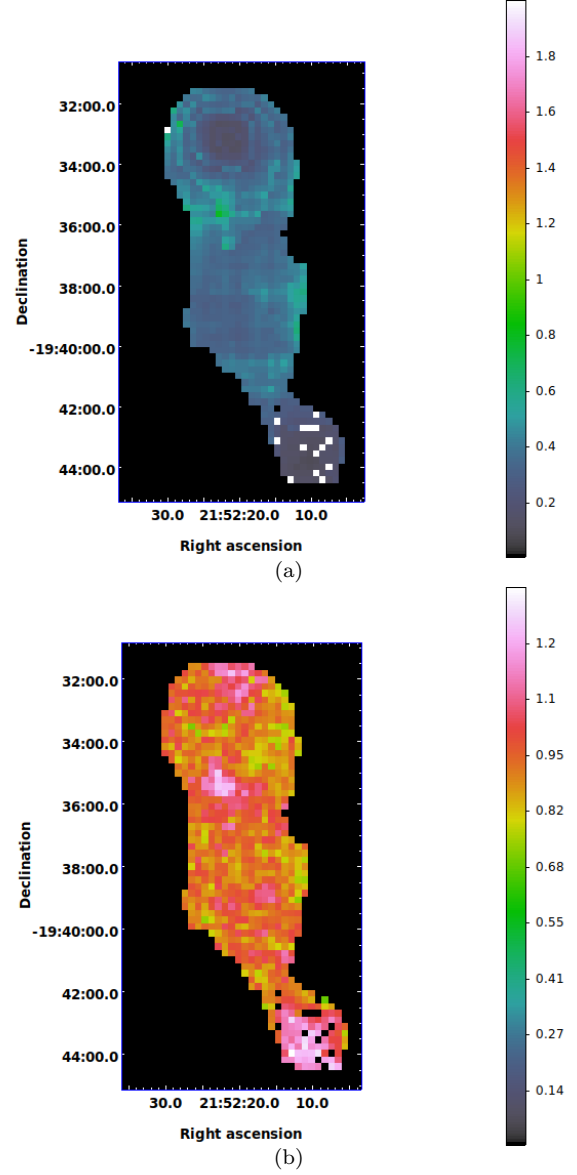


Figure 1: (a) XMM-Newton temperature error map in unit of keV. (b) Reduced χ^2 map of temperature map.